ADVANCED MATERIALS
www.advmat.de

4D-Printed Soft and Stretchable Self-Folding Cuff Electrodes for Small-Nerve Interfacing

*Lukas Hiendlmeier, Francisco Zurita, Jonas Vogel, Fulvia Del Duca, George Al Boustani, Hu Peng, Inola Kopic, Marta Nikić, Tetsuhiko F. Teshima, and Bernhard Wolfrum**

Peripheral nerve interfacing (PNI) has a high clinical potential for treating various diseases, such as obesity or diabetes. However, currently existing electrodes present challenges to the interfacing procedure, which limit their clinical application, in particular, when targeting small peripheral nerves (<200 µm). To improve the electrode handling and implantation, a nerve interface that can fold itself to a cuff around a small nerve, triggered by the body moisture during insertion, is fabricated. This folding is achieved by printing a bilayer of a flexible polyurethane printing resin and a highly swelling sodium acrylate hydrogel using photopolymerization. When immersed in an aqueous liquid, the hydrogel swells and folds the electrode softly around the nerve. Furthermore, the electrodes are robust, can be stretched (>20%), and bent to facilitate the implantation due to the use of soft and stretchable printing resins as substrates and a microcracked gold film as conductive layer. The straightforward implantation and extraction of the electrode as well as stimulation and recording capabilities on a small peripheral nerve in vivo are demonstrated. It is believed that such simple and robust to use self-folding electrodes will pave the way for bringing PNI to a broader clinical application.

1. Introduction

Peripheral nerve interfacing (PNI) is a promising tool in medicine. It can be used to elicit specific responses in the body by stimulating the nerves. At the same time, PNI can be used for reading sensory or motor signals via electrical recording of compound action potentials. PNI is already clinically applied, for example, to treat depression and epilepsy by stimulating the vagus nerve or providing sensory feedback to neuroprostheses.[1–4] Furthermore, it is expected that more diseases and health conditions in the future can be targeted with PNI-based treatments, complementing and eventually substituting drug therapies and their side effects. Examples of future applications are the neuromodulation of the kidney to regulate blood pressure, treatment of diabetes, and fat tissue regeneration.[5–9]

Current clinical applications target the larger nerves of the body, typically in the mm range. Such nerves comprise many axons, and it is currently challenging to interface specific fibers in isolation from the rest. On the other hand, small nerves are found near their target tissue and usually comprise fewer axons. Therefore, it is possible to increase selectivity in stimulation and recording by interfacing small nerves. However, these nerves are usually a few tenths to hundreds of µm in diameter, which demands the use of electrodes of a correspondingly small size. Yet, the development of small electrodes increases the challenges to their design and implantation.[10,11]

Different electrode designs have been developed for PNI. Intraneural electrodes are inserted into the nerves; and therefore, achieve good spatial selectivity for stimulation and recording because the electrodes lie in close proximity to the nerve fibers (e.g., the TIME electrode).[12,13] Nevertheless, intraneural electrodes generate nerve trauma because they pierce through the nerve tissues during the insertion, either because of the stiffness of the shuttle that guides the electrode inside the nerve or because of the stiffness of the electrode itself (e.g., the Utah-array).[14,15] The development of trauma and foreign body reaction causes these electrodes to decrease in performance after a short time, currently restricting their use to the research field. Furthermore, the invasive interfacing procedure usually limits their application to larger nerves.[14] On the other hand, cuff electrodes, a subset of extraneural electrodes, are placed around the nerve for interfacing. Such electrodes are intrinsically less selective than intraneural electrodes but have the advantage of reduced invasiveness, which is beneficial for clinical applications. As they do not penetrate the nerve tissue,

L. Hiendlmeier, F. Zurita, J. Vogel, F. Del Duca, G. Al Boustani, H. Peng, I. Kopic, M. Nikić, T. F. Teshima, B. Wolfrum
Neuroelectronics
Munich Institute of Biomedical Engineering
School of Computation, Informatics and Technology
Technical University of Munich
Hans-Piloty-Str. 1, 85748 Garching, Germany
E-mail: bernhard.wolfrum@tum.de

L. Hiendlmeier, F. Zurita, F. Del Duca, G. Al Boustani, T. F. Teshima, B. Wolfrum
Medical & Health Informatics Laboratories
NTT Research Incorporated
940 Stewart Dr, Sunnyvale, CA 94085, USA

The ORCID identification number(s) for the author(s) of this article can be found under https://doi.org/10.1002/adma.202210206.

DOI: 10.1002/adma.202210206

they cause less nerve trauma in comparison to intraneural electrodes. Nerve trauma can be further mitigated by reducing the mechanical mismatch between the cuff and the nerve via carefully selecting the fabrication materials. Currently, the materials of choice for electrodes are either soft and stretchable materials, such as hydrogels and silicone elastomers,[16–20] or conformal thin film materials, such as polyimide and parylene.[21–24] Thin film electrodes achieve a smaller aspect ratio than elastomers but are typically more challenging to handle.

One decisive factor in the performance of the cuff electrodes both for stimulating and recording is their proximity to the surface of the nerve. Hence, the attachment mechanism of the electrode to the nerve plays a fundamental role. Cuff electrodes are often manually interfaced and attached to the nerves through suturing, clips, or zip tie-like mechanisms.[10,11,25–27] Other cuff electrodes are already pre-folded using fabrication-induced stress and have to be manually unfolded during the attachment, where they then wrap themselves around the nerve when released.[28–30] The difficulty of this procedure further increases with the reduction of the cuff size. Thus, a manual operation on smaller and more delicate nerves brings along an increased risk of nerve damage. Consequently, new methods are being investigated to interface cuff electrodes to small nerves. Current approaches include electrodes glued to the neuronal tissue to avoid mechanical attachment mechanisms or actuated electrodes, which deform and wrap around the nerve during the implantation on a specific trigger.[31,32] For example, a pneumatically-actuated electrode is developed for the central nervous system, which unfolds from a rolled state under pressure.[33] Other cuff electrodes are based on shape memory polymers, which can be flattened before insertion and then fold back when heated up to body temperature. Those cuffs have been used to interface nerves with diameters in the millimeter range.[34,35] Furthermore, there are cuff interfacing approaches, which use a bilayer of a swelling and a flexible material to generate the folding of the electrode around the nerve when in contact with water.[36] In principle, this approach can achieve folding diameters of ≈50 µm.[37]

Using an engineering approach, we aimed at providing a tool for researchers and surgeons to investigate the possibilities of interfacing small peripheral nerves. To this end, we developed a 4D-printed electrode for acute small peripheral nerve interfacing with a structure that allows its self-folding to a nerve cuff during the insertion. It features a custom-developed hydrogel material, which swells when in contact with water and serves as the actuation mechanism once the device is inserted. Our device is easy to handle and with intrinsic stretchability for applications in which this characteristic is required. We demonstrated reliable interfacing of small nerves (≈150 µm) in vivo and successful stimulation and recording of neural signals. Furthermore, we also showed that the electrodes are straightforward to extract without damaging the nerve.

2. Results

2.1. 4D-Printed Electrode

To simplify the interfacing procedure of cuff electrodes on small peripheral nerves, we designed a device that can leverage on the swelling properties of a water-absorbent hydrogel material. Contact with fluids, such as body fluids, triggers a self-folding mechanism, causing the cuff electrode to wrap around the nerve (**Figure 1**a,b). Hydrogels are a class of materials that can absorb significant amounts of water, swelling when they get wet and shrinking when they dry. Swelling in water proved to be a suitable actuation strategy because nerves are usually found in aqueous environments.[37,36] Therefore, we use this material behavior as the driving force for the folding. Many hydrogels are also biocompatible and some have been additionally modified to be 3D printable.[38,39] We chose 3D printing as the fabrication method because it provides freedom in design and the possibility of combining different materials, including soft, flexible, and active ones like hydrogels.[40] The use of active materials, which deform under certain conditions, is commonly referred to as 4D printing.[41–43] Thus, we call the self-folding electrodes "4D electrodes". Our devices consist of a bilayer structure, comprising of a non-swelling flexible material and a highly swelling hydrogel on its backside as the substrate. Both layers are printed subsequently using frontal photopolymerization (FPP) in a stereolithographic 3D printer. The non-swelling layer is printed using a commercially available flexible polyurethane photocurable printing resin (flex resin). As the swelling hydrogel, we used a super absorbent 3D printing resin based on sodium acrylate.[44] When in contact with water, the superabsorbent material swells and exerts a force that bends and folds the inner layer formed by the flex resin. Compared to other printable hydrogels, the super absorbent resin has the advantage of being patternable in an almost dried state, showing a high swelling ratio and exerting sufficient force during the deformation. These properties make it possible to achieve the desired folding diameters for small PNI (100–200 µm), as shown in Figure 1c–g. Structuring the superabsorbent layer as stripes perpendicular to the folding hinge ensures directing of the force of the swelling in the folding direction. The patterning and material selection result in an electrode that is soft, stretchable, biocompatible; and therefore, appropriate to interface with small nerves without damaging them (biocompatibility data can be found in Figure S3, Supporting Information). As both materials are acrylate-based 3D printing resins, they covalently bond together after being postcured. The resulting adhesion is necessary to generate the stress due to the unequal swelling of the layers, which is released during folding. Last, a conductive Ti/Au layer is sputtered on top of the self-folding substrate, so that the metal is on the inner surface of the cuff and laser-patterned to form feedlines with a width of 100 µm. We passivated the feedlines by spin coating a layer of the flex resin up to the folding tip of the cuff electrode. Figure 1i showcases two, four, and six electrode devices after passivation.

A primary advantage of the FPP printing method is that we can easily combine the two materials while having precise control over the geometry and the thickness of the different layers by simply exposing the areas in the liquid resin for different durations. The contact pads were fabricated thicker (250 µm) than the rest of the electrode to connect with standard FPC/ZIF connectors. The body of the electrodes was 150 µm thick to be flexible and stretchable; and therefore, easy to handle, while the folding hinges were thinner (50 µm) to present lower mechanical resistance while bending. We also controlled the

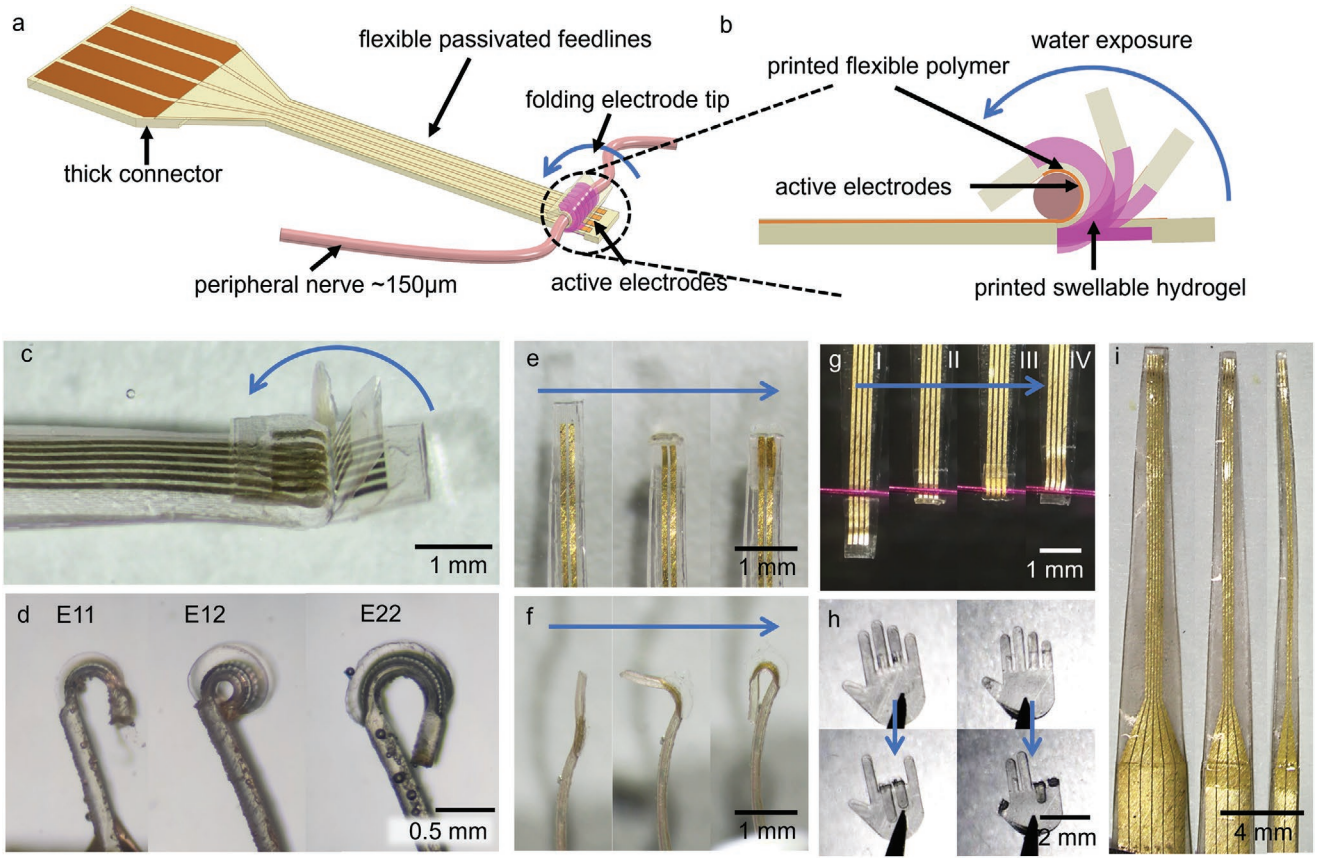

Figure 1. 4D-printed self-folding electrode. a) Schematic overview of the whole cuff electrode from the contact pads to the foldable tip that attaches to the nerve. b) Schematic close-up side-view of the electrode tip, showing the changes of the layers at different steps of the folding. c) Perspective view of the cuff electrode, obtained by overlaying multiple images during the folding in water. d) Lateral view of the cuff electrodes fabricated with different layer thicknesses: E11 both layer thin, E12 increased swelling layer thickness, and E22 both thicknesses increased. e,f) Top and lateral view of the folding of the tip of a two-electrode device after immersing in water, from left to right. g-I–II) Electrode wrapping around a wire and opening when being pulled off while measuring the force required to open (III–IV). h) Top to bottom folding of the fingers on a hand upon water exposure, with two different designs. i) Devices featuring two, four, and six electrodes.

thickness of the superabsorbent layer by the exposure dose to achieve controlled folding diameters. By adjusting the thickness of the layers, we could tune the folding diameters to different dimensions to fit to several sizes of small nerves, as shown in Figure 1d and for a wider range (Figure S1, Supporting Information). As long as the nerve diameter does not exceed the cuff diameter, no compression force is applied on the nerve, which prevents damage to the neural tissue. For larger nerves, the compression can be approximated by the maximum force required to open the cuff (see Table S1, Supporting Information). A crucial advantage of this printing method is that the different thicknesses can be printed entirely on the same structure, combining contact pads, main body, and bending hinge in a single unit; thus, minimizing the complexity of the fabrication and increasing the reliability of the device.

Tuning the folding parameters also allows us to control the force required to extract the electrode from the nerve without damage by just pulling it off. **Table 1** presents the mechanical characteristics for some cuff electrodes. For example, the electrode labeled E11 (Figure 1d) has the thinnest layers of the three presented cuff electrodes, fabricated at an exposure time of 1.5 s for the flex resin layer and 18 s for the superabsorbent layer. When the thickness of the superabsorbent layer increases, as in E12 (1.5 s exposure for the flex resin and 28 s exposure for the superabsorbent layer), the folding diameter decreases, and the required opening force increases. An additional increase in the thickness of the flex resin layer with 4.5 s and 48 s in the superabsorbent (E22) increases the folding diameter along with the required opening force. Such fine control over the printing means this fabrication technique can be easily extrapolated to produce more complex structures with several folding

Table 1. Influence of printing parameters on the layer thicknesses ($n = 4$) and the resulting different folding diameters ($n = 4$) as well as the maximum forces ($n = 8$) needed to open the electrodes, per unit length of the cuff.

	E11	E12	E22
Thickness flex resin	48 ± 5 µm	48 ± 5 µm	91 ± 15 µm
Thickness SAP resin	19 ± 13 µm	62 ± 15 µm	43 ± 14 µm
Folding diameter	260 ± 57 µm	147 ± 25 µm	366 ± 52 µm
Opening force per interfaced length	18 ± 6 mN mm^{-1}	33 ± 7 mN mm^{-1}	65 ± 8 mN mm^{-1}

parts. To illustrate this point, we print tiny hands with several folding fingers just by changing the structure design, as shown in Figure 1h. This freedom in design and straightforward control of the mechanical properties can be further leveraged to produce interfacing electrodes for multiple nerves in a single device.

2.2. Stretchability

The desirable characteristics of PNI electrodes include ease of handling and robustness to facilitate their implantation to the practitioner. Our goal was to design the cuff electrodes to be flexible and stretchable up to 20% without rupture so that they could be handled and bent freely during surgery. The flex resin allows the substrate to stretch with an elasticity modulus of 5.8 ± 0.7 MPa, shown in the stress–strain curve in **Figure 2**a. The mechanical characterization of the superabsorbent material is shown in the Figure S2, Supporting Information.

Electrodes made with thin metal layers often degrade in electrical performance when stretched or under applied pressure due to failure of the metal layer. However, our electrodes overcome this issue by forming microcracks. Microcracking is a technique that achieves conductive stretchable thin films

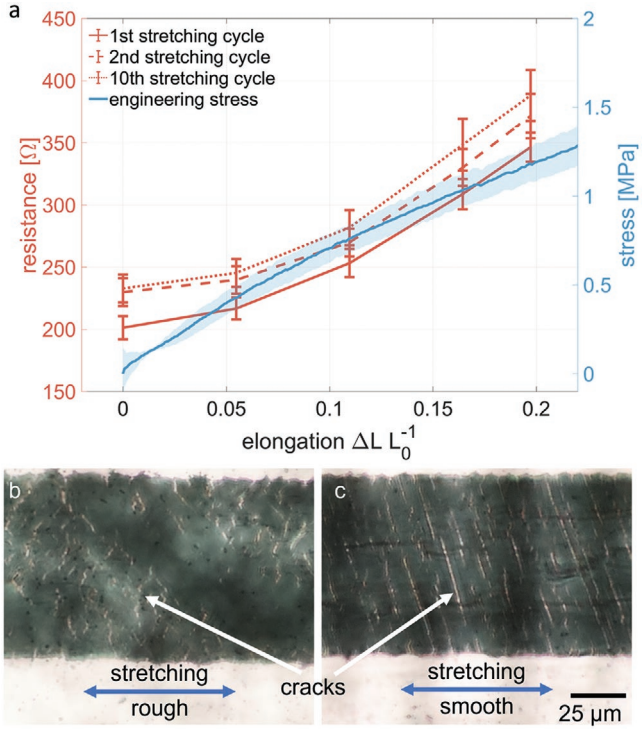

Figure 2. Stretchability of the electrode feedlines. a) Orange lines: conductivity of electrodes fabricated with a rough structure during stretching cycles up to 20% in length, mean and standard deviation (n = 11). Blue curve: engineering stress of the electrode during the stretching, mean, and standard deviation (shaded n = 8). b,c) Representative bright-field image of the Au feedline at 20% elongation in feedline direction: fabricated on a rough surface, showing random cracks in the layer, leaving still connected Au islands (b), fabricated on a smooth electrode surface, showing straight cracks through the feedline resulting in not reproducible conductivity measurements even in the unstretched state (c).

where small random cracks are introduced.[45,46] Compared to the large cracks usually formed during the stretching of metal films, microcracking forms small metal islands, which provide a conducive path through the metal layer even when stretched. The microcracking was implemented by depositing the Ti/Au layer on a roughened surface. Owing to the local stress introduced by the roughness, the microcracks formed evenly scattered during the initial strain cycles instead of larger cracks like in smooth films, keeping the conductivity of the feedlines. The transmitted-light images in Figure 2b showcase the microcracks in the Ti/Au layer at 20% strain. For comparative purposes, we fabricated the same electrodes using a smooth surface and confirmed the development of cracks extending across the stretched feedline, disrupting the conductivity (Figure 2c). To further assess the change in conductivity of both fabrication methods, we performed resistivity measurements while simultaneously stretching the electrodes. The resistivity of the feedlines fabricated on the rough surface increased with the stretching, as shown in the conductivity-strain curve in Figure 2a. However, when the electrodes were released, the resistance decreased to a value slightly higher than the initial one. After a series of stretching cycles, the resistance at 0% strain stabilized at ≈230 ± 10 Ω as no further cracks formed on the feedlines. In comparison, the resistivity of the electrodes manufactured on the smooth surface could not be reliably measured, even unstretched, probably because the big cracks had already formed during the manufacturing process or their subsequent handling. These results show that the rough surface could successfully introduce microcracks and retain the metal films' conductivity during stretching. Although we did not test the electrode behavior at a constant stretch when implanted in the body over the long term, we believe this test shows that the electrodes are robust enough to withstand manipulation during surgery.

2.3. Electrochemical Characterization

We characterized the impedance of the electrodes using electrochemical impedance spectroscopy (EIS). Typically, a low electrode impedance is desirable for stimulation to deliver the necessary amount of charge while minimizing the polarization of the electrodes. A high electrode polarization could elicit redox reactions on the surface of the electrodes, which generate noxious species or degrade the performance of the electrodes. To assess the influence of stimulation on the electrode performance, we compared the impedance of n = 16 electrodes before and after applying 1 million stimulation pulses. The EIS was conducted in a three-electrode setup, with the Ti/Au electrode set as the working electrode, a Pt mesh counter electrode, and an Ag/AgCl (3 M NaCl) reference electrode. The measurement was performed in phosphate-buffered saline (PBS). The Bode plots for both cases are compared in **Figure 3**a, where the results show that the average magnitude of the impedance of the electrodes increased slightly after the stimulation; however, not significantly. For example, at 1 kHz, the magnitude of the impedance increased from ≈6 kΩ to ≈10 kΩ, and similar changes were seen across all measured frequencies. This result is expected, as the stimuli could have briefly generated

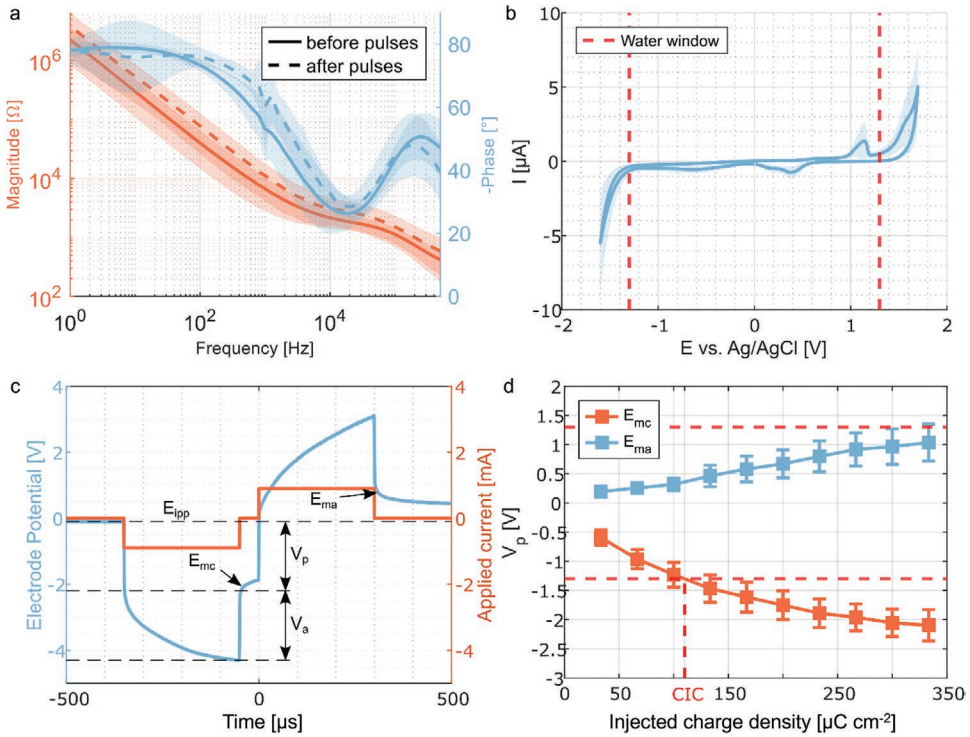

Figure 3. Electrochemical characterization of the active electrode in PBS. a) Bode plots of the impedance of the electrodes in PBS depicted as the mean and the standard deviation of $n = 16$ electrodes. The solid and dashed lines show the EIS before and after delivering 10^6 biphasic current pulses, respectively. b) CV of $n = 16$ electrodes scanned at 50 mV s^{-1}. We determine the water window to be at ±1.3 V. c) Representative voltage transient resulting from a 0.9 mA biphasic stimulation pulse. Here, we showcase the relevant voltage values to calculate the electrode's charge injection capacity (CIC). This trace corresponds to an injected charge density of 300 µC cm^{-2}. d) The charge injection density of $n = 16$ electrodes, shown in mean and standard deviation. The charge injection capacity is estimated to be 121 µC cm^{-2}.

gas bubbles between the Au microcracks, delaminating some weakly attached Au.

We conducted cyclic voltammetry (CV) measurements to further characterize the electrodes' stability and determine the safe stimulation limits where hydrolysis of water did not occur, that is, determine the water window. The mean and standard deviation of the voltammograms (n = 16) for Au versus Ag/AgCl (3 M NaCl) with a Pt mesh counter electrode in PBS are shown in Figure 3b. The high current magnitudes at the highest and lowest applied voltages correspond to water hydrolysis. Therefore, we set a conservative water window in the range of ±1.3 V. Lower current peaks could be noticed at ≈1.1 V (anodic) and ≈0.6 V (cathodic) versus Ag/AgCl, probably corresponding to the oxidation and reduction of Au, respectively.

The electrode's charge injection capacity (CIC) determines how much charge can be injected into the electrolyte without polarizing the electrode beyond undesired limits. We set the water window as the safe stimulation limit in our case. Keeping the electrode polarization within the water window minimizes or prevents the generation of H_2 (g) and O_2 (g), which are undesired reaction products and can diffuse away from the electrode surface into the body. In Figure 3c, we show a characteristic trace of the voltage response of the electrode to a balanced biphasic current pulse. We can analyze this voltage response to determine the most cathodic (E_{mc}) and anodic (E_{ma}) electrode polarization and contrast them with the previously established water window. Determining these voltage levels from a voltage transient is challenging, and there are even attempts to automate their calculation.[47] The resulting voltage transient after application of a current stimulus can be separated in the near-instantaneous voltage change generated mainly by the ohmic resistance of the electrolyte, also called access voltage (V_a), and the electrode polarization voltage (V_p), referenced to the potential before the stimulus is applied, called interpulse potential (E_{ipp}).[48] To estimate E_{mc} and E_{ma}, we stimulated the $n = 16$ electrodes with cathodic-leading biphasic pulses of increasing amplitude ranging from 100 to 1000 µA. We converted the injected current to the surface charge density as $Q_{inj} = (I_{inj} \times t_p)/A$, where Q_{inj} represents the injected surface charge density, I_{inj} the stimulation current amplitude per phase, t_p the phase duration, and A the electrode area. Mean and standard deviation of the corresponding E_{mc} and E_{ma} estimations are presented in Figure 3d using a fit of the discrete values with a quadratic regression. We finally estimated the CIC as the injected charge corresponding to the intersection between the first polarization voltage E_{ma} or E_{mc} and the established water window, obtaining a CIC of 121 µC cm^{-2}. These values are slightly lower but in the same order of magnitude as results reported in literature for Au electrodes (200 µC cm^{-2}).[49] The reduced CIC compared to flexible but non-deformable electrodes can be caused by the microcracking design. For applications requiring higher CICs, the performance could be potentially improved with an additional coating of a porous conductive polymer, such as PEDOT:PSS.[49,50]

2.4. In Vivo Validation

We interfaced a nerve of the locust *Locusta migratoria* to validate the in vivo performance of the 4D cuff electrodes. The nerve 5 (N5) emerges from the locust's metathoracic ganglion and innervates the animal's hind leg. It comprises many afferent (toward the ganglion) and efferent (toward the leg) nerve fibers, including the ones responsible for jumping (**Figure 4**a). It is a small nerve of ≈150–200 µm in diameter, and the length for interfacing inside the metathoracic cavity is usually limited to only a few mm. These small dimensions make the locust's nerve an excellent model to show the interfacing of small peripheral nerves in limited space. The cuff electrode we present has six channels and is 850 µm in width. However, making a multichannel planar electrode with the appropriate dimensions for a small nerve in a restricted environment is only half the story. Interfacing with small nerves usually requires a great deal of skill from the practitioner. Commercially available cuff electrodes are traditionally fixed to the nerve by stitching or buckling around them, which is more challenging at smaller scales (e.g., CorTec GmbH, Freiburg, Germany, MicroProbes, Gaithersburg, MD, USA). Our self-foldable cuff electrodes are comparatively easy to attach to the nerve, as they just need to be approached to it, wrapping around it after contact with water in 20 to 30 s (Figure 4d–f).

2.4.1. Stimulation

To validate the stimulation capabilities of the 4D cuff electrode, we stimulated the nerve with biphasic current pulses and recorded the elicited leg response on camera. The pulses were delivered between two electrodes every 2 s. The stimuli triggered the leg's fast extensor tibiae neuron (FETi), provoking it to extend its tibiofemoral joint.[51] Figure 4c showcases one stimulation experiment comprising ten stimulation pulses and showing the tibiofemoral joint angle versus time, with similar values for every stimulation pulse. Repetitions of the same experiment in other subjects showed a variability in the elicited angle span between the subjects but repeatability within the same subject. This can be attributed to the position of the electrode with respect to the nerve and its proximity to the FETi, which varied between subjects.

2.4.2. Recording

In addition to the stimulation, we evaluated the recording capability of the electrodes. After nerve attachment, we could detect spontaneous neural activity, which was always present even without movement, probably corresponding to sensory signals.

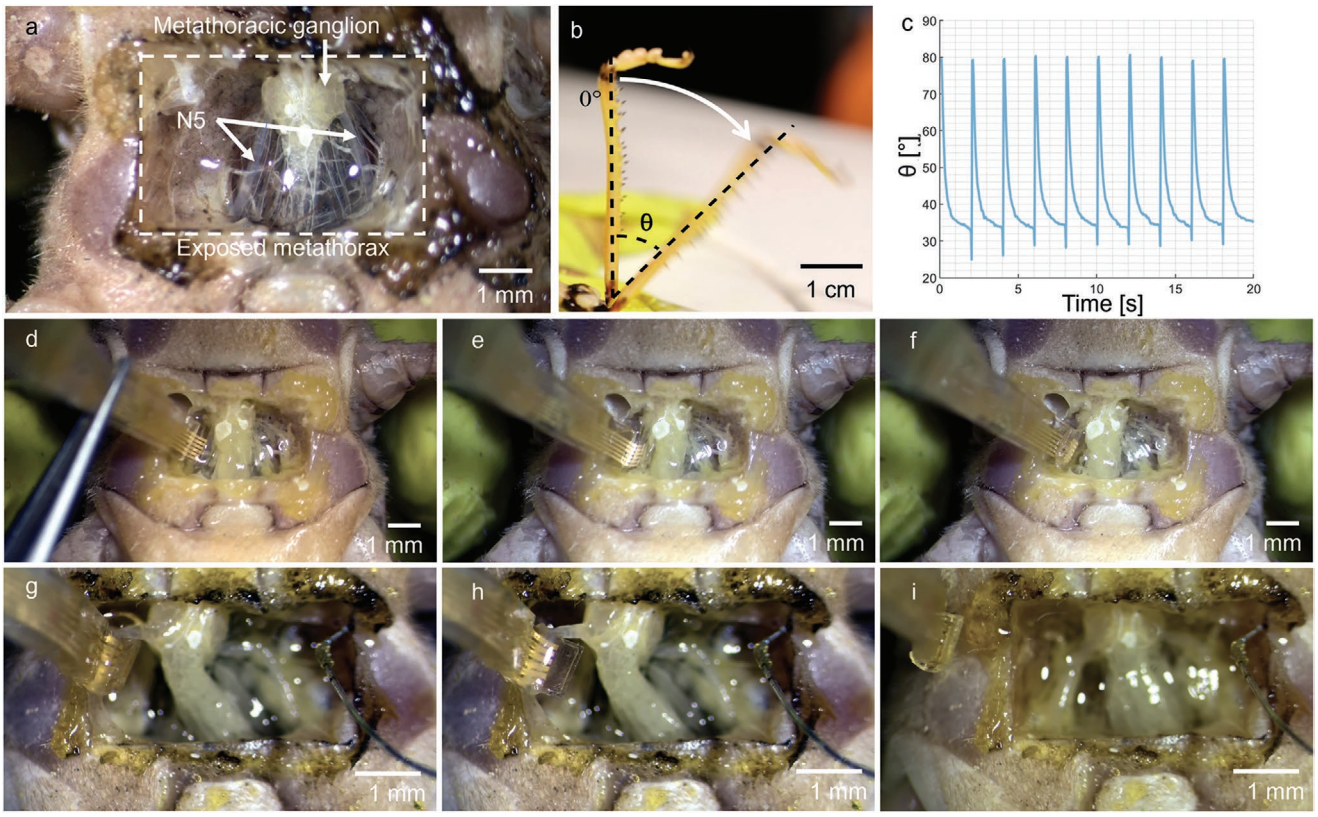

Figure 4. Interfacing of the locust N5 with the 4D cuff electrode. a) Metathoracic cavity of a locust, exposing the metathoracic ganglion and nerves. b) Movement of the hindleg elicited by the nerve stimulation. c) Angle of the leg over ten stimulation pulses. d–f) Electrode insertion sequence. The unfolded cuff electrode is placed next to the nerve (d). In contact with the electrolyte, the superabsorbent polymer swells, causing the substrate to fold and subsequently wrap around the nerve (e). After fully folding, the Au electrodes are in contact with the nerve and can be used for recording and stimulation (f). g–i) Through adjusted printing parameters, the electrode's opening force can be adjusted to pull the electrode off the locust without rupturing the nerve. The electrode can just be pulled via the feedline. As a consequence, the cuff opens, releases the nerve, and then snaps back in its closed position.

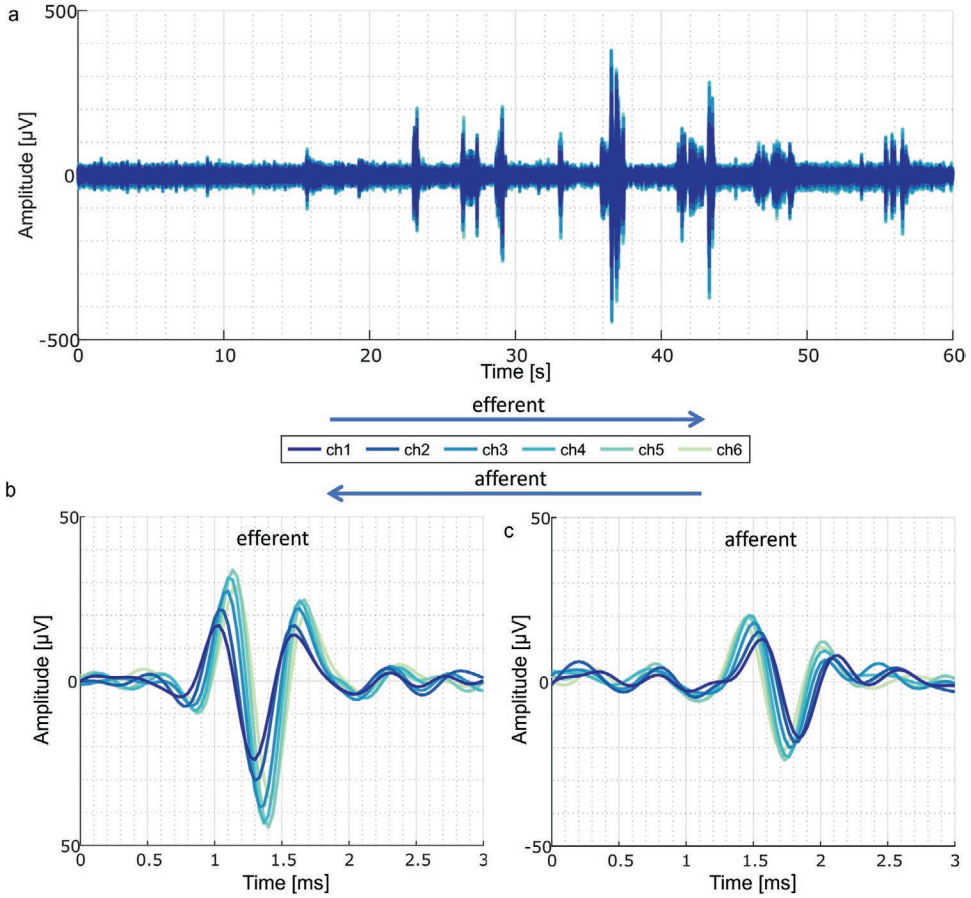

Figure 5. Electrophysiological recordings of spontaneous activity of the N5 with a six-channel cuff electrode. a) Activity during 1 min; the larger spikes correspond to leg movement. b,c) Zoomed-in snippets from the main trace at different times show a motor signal traveling from the ganglion to the leg (efferent) (b) and a sensory signal traveling from the leg to the ganglion (afferent) (c). The direction of propagation of the signal can be determined from the observed phase delay between the different channels, with the most proximal channel (ch1) leading during efferent activity (b) and lagging during afferent activity (c).

Then, we elicited movement by lightly touching the abdomen of the locust. Correspondingly, the sudden movement of the leg was reflected as larger and bursting neural activity. A representative trace of the recording is shown in **Figure 5**a. The signal was band-pass filtered between 0.8 and 2.2 kHz to reduce noise and muscle movement artifacts.[52–54] After filtering, the noise floor was calculated to be ≈4 μV_{rms}. Traditional extra-neural recording techniques, such as interfacing with hook electrodes, usually record action potentials with higher amplitudes when the nerve is pulled out of the hemolymph. Nevertheless, it is important to highlight that the presented recordings were performed with the electrode immersed in the animal's hemolymph, a condition for implantable electrodes that hook electrodes cannot meet. Furthermore, the geometrical arrangement of the six-channel cuff electrode permits the distinction of the direction of propagation of the neural activity along the nerve, depending on the dephasing profile, with electrodes 1 to 6 (ch1–ch6) going in the proximal to distal direction. Figure 5b shows a ch1-leading signal, corresponding to efferent motor neural activity, while Figure 5c depicts a ch6-leading signal, corresponding to afferent sensory neural activity. In one minute of the shown trace, 218 efferent and 129 afferent signals were detected. Data from further interfaced nerves can be found in the Supporting Information.

2.4.3. Extraction

During the experiment, the cuff electrode moved along with the nerve and did not detach when the animal stirred. However, when the cuff is pulled more strongly, it can unfold again. Using this property, the cuff electrodes were detached from the nerve after every experiment simply by gently pulling them off (Figure 4f–h). We repeated this procedure six times on different nerves, and the videos of the extraction can be found in the Supporting Information. In all cases, leg movement was normally elicited as a response to light touches on the abdomen of the locust after extraction of the cuff electrode. This observation suggests that the interfacing and the extraction cause little or no damage to the nerve. The electrode's opening force can be controlled by tuning the fabrication parameters to adjust to different nerves.

3. Conclusion and Outlook

We have reported a 3D-printed electrode for PNI, which can fold itself into a cuff around small peripheral nerves (100–200 µm) when exposed to water during the surgery. The materials used for the fabrication make the electrode robust and easy to handle. Furthermore, we confirmed that triggered self-folding mechanisms greatly facilitate the interfacing procedure for the surgeon compared to other devices. We believe this simple handling is key to bringing PNI into a broader clinical application. Last, we showed that the electrode can reliably stimulate small nerves and perform electrophysiological recordings from them.

The successful in vivo results on insects suggest that acute functional interfacing of our devices is possible. The materials used for the electrode fabrication have already been shown to be cytocompatible in the literature.[44,55] However, their long-term behavior in vivo has not been yet extensively tested, as it has been done for other electrode materials, such as parylene, silicones, and polyimide. Therefore, the next steps should include long-term biocompatibility analyses of foldable devices implanted in small mammals including assessment of foreign body reaction and material stability.

4. Experimental Section

Materials: The flexible 3D printing resin luxaprint flex (flex resin) was purchased from Detax (Germany). Acrylic acid, 2-hydroxyethyl methacrylate (HEMA), sodium hydroxide (anhydrous; NaOH), poly(ethylene glycol) diacrylate (PEGDA, M_n 525), 2,2,6,6-tetramethylpiperidine-1-oxyl (TEMPO), and modified Dulbecco's PBS were obtained from Sigma–Aldrich (USA). B(2,4,6-trimethylbenzoyl) phenylphosphine oxide/ethyl(2,4,6- trimethylbenzoyl) phenyl phosphinate (Omnirad 2100) as photoinitiator blend and 2-isopropylthioxanthone (ITX) as UV-absorber were purchased from IGM Resins (The Netherlands). 2-Propanol (≥99.5%) and ethanol (≥99.5%) were obtained from Carl Roth (Germany). Deionized water was generated by an Ultra Clear purification system (Evoqua Water Technologies, Germany). $76 \times 52 \times 1$ mm^3 microscopy slides (Marienfeld) were purchased from VWR (USA). Locust ringer solution was prepared from 147 mM NaCl, 10 mM KCl, 4 mM CaCl2, 3 mM NaOH, and 10 mM HEPES buffer (Sigma–Aldrich, USA). The locusts were purchased from a local animal store.

Electrode Fabrication: The bilayer as the substrate of the self-folding electrode was fabricated by frontal photopolymerization (FPP) of 3D printing resins.[56,57] This method is a variation of vat polymerization 3D printing. A thick layer of liquid photosensitive resin was thereby exposed by a structured light source from the bottom to generate a solid structure. However, in contrast to conventional 3D printing, multiple layers were not attached to each other; instead, only the first layer was used. The photoabsorber in the resin attenuated the light from the bottom, limiting the polymerization thickness. The thickness could be fine-tuned by a change of exposure time or UV light intensity. Thus, this method allows printing flat structures composed of parts with different thicknesses.

The bilayer was composed of two materials: First, a commercial biocompatible flex resin was used to create a flexible base layer. To the bulk resin, 0.4% w/w ITX was mixed as UV absorber to gain better control over the thicknesses in the required range (50–300 µm) during FPP. Second, a previously reported superabsorbent resin, with slightly modified composition, was used for the swelling layer.[44] It was composed of acrylic acid neutralized with 30% NaOH to a degree of 37%, 26% HEMA, 5% PEGDA 525 as crosslinker, 1% Omnirad 2100 as photo initiator, 0.2% ITX as photo absorber for thickness control, and 0.01% TEMPO as polymerization quencher (w/w). The resins were exposed on a Miicraft 50 × 3D printer (Miicraft, Taiwan) from the bottom through a roughened glass slide as carrier ($76 \times 52 \times 1$ mm^3, 6.2 mW cm^{-2}, 365 nm wavelength). The exposure time was controlled to achieve different substrate heights by converting the CAD model (Inventor 2022, Autodesk, USA) into a print file using the printer's Miiutility software (Miicraft, Taiwan), giving each structure its layer with a specific exposure time. First, the flex resin on top of the roughened glass slide in the folding hinge for 1.5 s (if not mentioned otherwise) was exposed to form a thin, easily foldable layer. The feedline part was exposed for 20 s and the contact pad area for 1 min to form a thick stable layer, as shown in **Figure 6**a. Next, the glass slide was washed with 2-propanol to remove uncured flex resin and it was placed again in the printer on the same position. Then, the SAP resin was applied on the folding hinge and exposed for 22 s in a pattern to form stripes with 150 µm width and 120 µm gap in between (Figure 6b). These stripes were necessary to guide the stress caused by the swelling into the folding direction. The uncured resin was washed off again, alternating with ethanol and DI-water, to prevent the swelling of the hydrogel. Last, the resulting solidified structures were fully cured in a UV-curing chamber under nitrogen flux with 2000 flashes (Otoflash G171, NK-Optic, Germany). This foldable bilayer was peeled off from the rough glass substrate and placed upside down with tape on a new glass carrier. Thereby, the rough structure of the glass substrate got transferred to the top of the inner surface of the folding bilayer (Figure 6c).

80 nm Au was sputtered to form the conductive electrode and feedline layer. Previously, a 10 nm Ti layer was sputtered on the substrate to enhance the Au adhesion (Moorfield nanoPVD, UK, 5×10^{-3} mbar argon, 12 W Au, 40 W Ti). Next, the Au electrodes on the substrate were patterned using a nanosecond pulsed laser scanner (MD-U1000, Keyence, Japan, 500 mm s^{-1} scan speed, 20% power, 80 kHz repetition rate). A flex resin passivation layer was spin-coated (Polo Spin 150i, The Netherlands, 1000 rpm, 30 s) onto the electrodes and cured again in the UV-curing chamber (Figure 6e). The active electrode sites and contact pads were previously masked with polyimide tape, which was removed after curing. Last, the batch of electrodes was released from the carrier and split into individual cuff electrodes using a scalpel. Grooves crafted by the polymerized flex resin structure guided the cutting along the electrode borders. They were subsequently stored for 24 h in PBS to remove possibly toxic uncured monomers and finally dried again to unfold.

The electrodes used in the experiments were fabricated with active electrode sites and feedlines of 100 µm in width with an interelectrode distance of 50 µm. On the six site electrodes, this resulted in an 850 µm-wide electrode tip. The contact pads were 450 µm wide with a pitch of 500 µm, which fit commercially available ZIF connectors. The electrodes had a total length of 24 mm and a 600 µm-wide folding hinge (if not stated otherwise). Each fabrication batch contained ten electrodes in one structure manually separated in the last step. The folding hand was fabricated similarly to the self-folding substrate of the electrodes but without the Au and passivation layers. It consisted of 400 µm-wide fingers, where the SAP polymer stripes were printed on the finger joints intended to fold.

Folding Diameters: To show how the layer thicknesses influence the folding of the electrodes, the bilayer was printed with different exposure times for the two materials. The electrodes labeled E11, E12, and E22 had exposure times of 1.5, 1.5, and 4.5 s for the hinge of the flex layer, and 18, 28, and 48 s for the superabsorbent layer, respectively. The electrodes with a smaller folding diameter (E11 and E12) were designed with a 450 µm-wide hinge, while the electrode F45_48 was designed with a 900 µm-wide hinge. The other shown cuff electrodes had a 600 µm-wide hinge. The thickness of the cured layers was measured ($n = 4$) with a laser profilometer (VK-X250, Keyence, Japan). The bilayers were immersed in water, and the folding was observed and recorded (R5, Canon, Japan) from the side of the electrodes under a microscope (BMS, The Netherlands). The recordings were subsequently analyzed with ImageJ (1.8.0_172). To measure the opening force required for unfolding the cuffing mechanism, the device was wrapped around a 200 µm thick wire in water and pulled off with a tensile tester (Zwick 2.5,

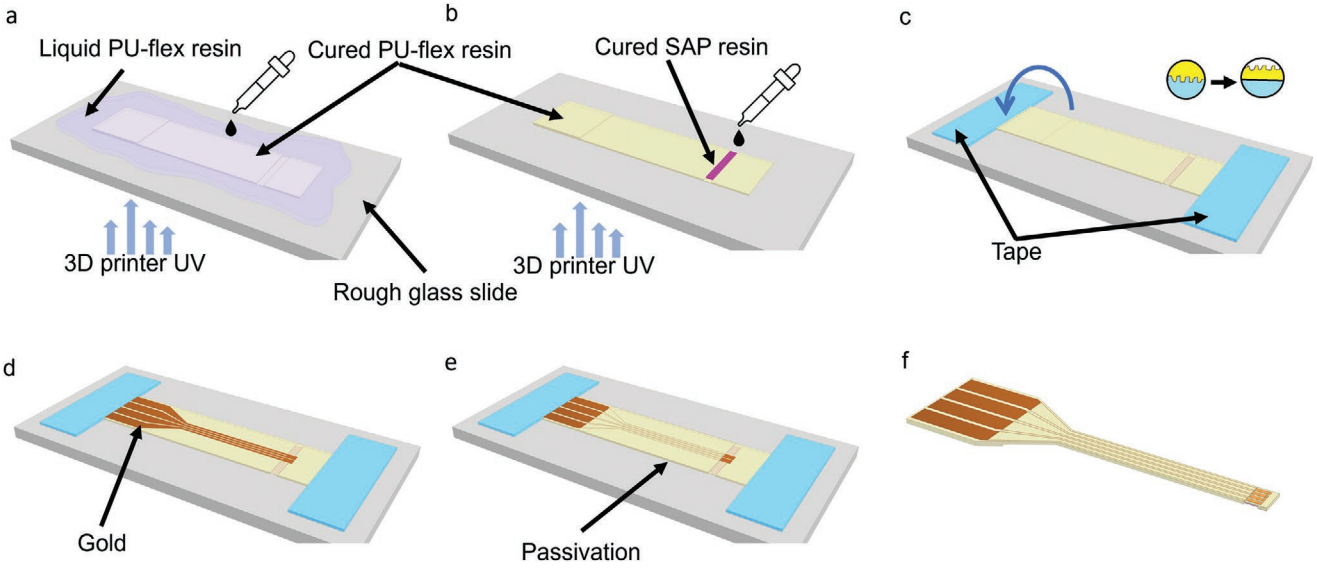

Figure 6. Schematic fabrication process of the electrodes. a) First, the flex resin was exposed through a roughened glass slide with a commercial 3D printer, to pattern the first layer of the substrate. b) After washing off the uncured flex resin, the superabsorbent resin was applied onto the cured flexible resin (yellow), again exposed (pink), and washed off. c) The printed bilayer structure was peeled off the glass slide and turned around. d) The conductive Au layer was sputtered onto this surface and patterned with a nanosecond pulsed UV laser. e) A flex resin passivation layer was applied by spin coating. f) The electrodes were manually chopped into the final shape.

Zwick-Roell, Germany) at 1 mm min^{-1} ($n = 8$), as shown in Figure 1g. The maximum force per unit length of the cuff was reported.

Stretching Characterization: To assess how the electrode stretching influences the conductivity of the Au layer, a custom linear displacement stage was built to fix the electrode in the stretched state. For uniform extension, the electrodes were cut in a rectangular shape during fabrication with a width of 3 mm. The microcracking was observed on a bright-field microscope (Axioskop 2, Zeiss, Germany). The electrode tip and the contact pads were electrically connected during the stretching to measure the conductivity of the feedlines (100 µm width, 14 mm length) (Fluke 287, Fluke, Germany). The device was stretched stepwise up to 20% and then rereleased to 0% strain for 1 min until the next stretching cycle was measured. 12 feedlines featuring a rough Au layer were successfully measured, while 24 feedlines of the electrodes with a smooth Au layer showed unreliable conductivity during the stretching cycles. The stress–strain relationship was determined with the same 3 mm-wide electrodes. They were pulled with a tensile tester (Zwick 2.5, Zwick Roell, Germany) from an initial length of 14 mm until rupture, with a strain rate of 14 mm min^{-1}, while keeping a temperature of 37 °C ± 5 °C.

Electrochemical Characterization: EIS and CV were performed to characterize the electrodes using a potentiostat (PalmSens4, PalmSens, The Netherlands) in PBS. EIS was performed in a three-electrode setup, using a Pt mesh counter and an Ag/AgCl (3 M NaCl) reference electrode. During the experiments, no bias voltage was applied against the open circuit potential (E_{oc}). A sinusoidal wave with an amplitude of 10 mV versus E_{oc} was applied to measure the impedance of the electrodes between 1 Hz and 500 kHz. CV was performed in the same three-electrode setup over a potential range of –1.6 to 1.7 V, with a scan rate of 100 mV s^{-1}. This voltage range was swept ten times, and only the last voltammogram was used for the data analysis.

The voltage response of the electrodes to biphasic current pulses was recorded with an oscilloscope (InfiniiVision DSOX2024A, Keysight, USA). The current pulses were applied with an electrophysiology stimulator/amplifier chip (RHS2116, Intan Technologies, USA) in the three-electrode setup described above. The phase of each pulse had a duration of 300 µs (leading cathodic) with a 50 µs interphase delay. The amplitude of the pulses ranged between 100 and 1000 µA in steps of 100 µA.

Animal Experiments: Adult male and female locusts (*L. migratoria*) were used for the in vivo experiments. As the study was conducted exclusively with insects, no special permission is required in Germany. All experiments complied with the German laws for animal welfare ("Deutsches Tierschutzgesetz"). The surgical procedure used was already described previously.[58] Before the surgery, the locusts were anesthetized by cooling them down to ≈2 °C for 30 min. Afterward, they were placed ventral side up on a modeling clay bed. The metathorax cuticle and the underlying air sacs and tracheae were removed to expose the metathoracic ganglion and the N5, a nerve comprising the fibers responsible for the fast extension of the hind tibia. Next, the cuff electrode was approached with the aid of micromanipulators and fine tweezers and wrapped around the nerve. The contact pads of the electrodes were interfaced to a six-pin zero insertion force (ZIF) connector (Würth Elektronik GmbH & Co. KG, Germany). This connector bridged the electrodes to an INTAN RHX control system, using the RHS2116 headset (INTAN Technologies, USA) to stimulate and record activity from the nerve. The locust's saline solution was applied to the thoracic cavity to prevent the nervous tissue from drying during the procedure.

The N5 was stimulated with two biphasic current pulses (leading cathodic, 10 ms apart) with an amplitude of 70 µA and a duration of 300 µs per phase, separated by a 100 µs delay between phases. The pulse was delivered every 2 s, and the leg movement response was captured on camera. The tibiofemoral joint angle was estimated using MATLAB (MATLAB 2022a, MathWorks, USA).

Last, the neural activity of the N5 was recorded from all channels at 30 ksps. The recording was performed against an Ag/AgCl electrode on the contralateral side of the metathorax. The abdomen of the animal was lightly touched with a non-metallic instrument to elicit a motor reaction. The acquired signals were subsequently processed using MATLAB. A FIR band-pass filter between 0.8 and 2.2 kHz was applied.[52]

Statistical Analysis: The number of repeated samples in each dataset was given with the data where the mean and standard deviation were calculated. To verify if the change of impedance before and after 10^6 stimulation pulses was significant, the distribution of the values at 1 kHz were checked using a Wilcoxon test (significance level $p < 0.05$), as the data was not normally distributed.

Ethical Approval: All animal experiments complied with the German laws for animal welfare ("Deutsches Tierschutzgesetz"). As the study was conducted exclusively with insects, no special permission is required in Germany.

Supporting Information

Supporting Information is available from the Wiley Online Library or from the author.

Acknowledgements

The authors acknowledge funding by the Federal Ministry of Education and Research (BMBF) and the Free State of Bavaria under the Excellence Strategy of the Federal Government and the Länder through the ONE MUNICH Project Munich Multiscale Biofabrication and the TUM Innovation Network: NEUROTECH.

Open access funding enabled and organized by Projekt DEAL.

Conflict of Interest

The authors declare no conflict of interest.

Author Contributions

L.H. and F.Z. contributed equally to this work. Designed the study: L.H., F.Z., and B.W. Prepared Figures 1, 2, and 6: LH. Prepared Figures 3–5: F.Z. Wrote the main manuscript text, with support from T.T. and B.W.: L.H. and F.Z. Designed and fabricated the devices: LH. Characterized them: L.H., F.Z., and J.V. Implemented them in vivo, processed, and analyzed the measurements: FZ. Helped to establish the fabrication techniques: F.D.D., G.A.B., H.P., I.K., and M.N. All authors reviewed the manuscript and provided critical feedback.

Data Availability Statement

The data that support the findings of this study are available from the corresponding author upon reasonable request.

Keywords

4D printing, cuff electrodes, hydrogels, nerve interfaces, self-folding, small nerves, stretchable materials

Received: November 3, 2022
Revised: December 19, 2022
Published online: February 11, 2023

[1] J. M. Bottomley, C. LeReun, A. Diamantopoulos, S. Mitchell, B. N. Gaynes, *Compr. Psychiatry* **2019**, *98*, 152156.
[2] J.-J. Fan, W. Shan, J.-P. Wu, Q. Wang, *CNS Neurosci. Ther.* **2019**, *25*, 1222.
[3] K. Kim, *Curr. Opin. Biomed. Eng.* **2022**, *21*, 100368.
[4] E. D'Anna, G. Valle, A. Mazzoni, I. Strauss, F. Iberite, J. Patton, F. M. Petrini, S. Raspopovic, G. Granata, R. Di Iorio, M. Controzzi, C. Cipriani, T. Stieglitz, P. M. Rossini, S. Micera, *Sci. Rob.* **2019**, *4*, eaau8892.
[5] A. F. Hoogerwaard, M. R. de Jong, A. Elvan, *Curr. Hypertens. Rep.* **2018**, *20*, 24.
[6] S. Helm, N. Shirsat, A. Calodney, A. Abd-Elsayed, D. Kloth, A. Soin, S. Shah, A. Trescot, *Pain Ther.* **2021**, *10*, 985.
[7] S. Kooijman, J. K. van den Heuvel, P. C. N. Rensen, *Trends Endocrinol. Metab.* **2015**, *26*, 657.
[8] K. Tan, Y. Lai, W. Chen, H. Liu, Y. Xu, Y. Li, H. Zhou, W. Song, J. Wang, K. Woo, Y. Yin, *J. Hum. Hypertens.* **2019**, *33*, 716.
[9] E. E. Meyers, A. Kronemberger, V. Lira, K. Rahmouni, H. M. Stauss, *Physiol. Rep.* **2016**, *4*, e12718.
[10] C. C. Rowan, O. Graudejus, T. M. Otchy, *Adv. Sci.* **2022**, *9*, 2102945.
[11] T. M. Otchy, C. Michas, B. Lee, K. Gopalan, V. Nerurkar, J. Gleick, D. Semu, L. Darkwa, B. J. Holinski, D. J. Chew, A. E. White, T. J. Gardner, *React. Fission Nat., C. R. Reun. Com. Tech.* **2020**, *11*, 4191.
[12] T. Boretius, J. Badia, A. Pascual-Font, M. Schuettler, X. Navarro, K. Yoshida, T. Stieglitz, *Biosens. Bioelectron.* **2010**, *26*, 62.
[13] V. Gaillet, A. Cutrone, F. Artoni, P. Vagni, A. Mega Pratiwi, S. A. Romero, D. Di Lipucci Paola, S. Micera, D. Ghezzi, *Nat. Biomed. Eng.* **2020**, *4*, 181.
[14] Y. Wu, L. Guo, in *Neural Interface Engineering: Linking the Physical World and the Nervous System* (Ed: L. Guo), Springer International Publishing, Cham, Switzerland **2020**, pp. 95–121.
[15] J. A. George, D. M. Page, T. S. Davis, C. C. Duncan, D. T. Hutchinson, L. W. Rieth, G. A. Clark, *J. Neural Eng.* **2020**, *17*, 056042.
[16] K. Terkan, F. Zurita, T. Jamal Khalaf, P. Rinklin, T. Teshima, T. Kohl, B. Wolfrum, *APL Mater.* **2020**, *8*, 101111.
[17] S. Lienemann, J. Zötterman, S. Farnebo, K. Tybrandt, *J. Neural Eng.* **2021**, *18*, 045007.
[18] Y. Liu, J. Liu, S. Chen, T. Lei, Y. Kim, S. Niu, H. Wang, X. Wang, A. M. Foudeh, J. B.-H. Tok, Z. Bao, *Nat. Biomed. Eng.* **2019**, *3*, 58.
[19] D. Afanasenkau, D. Kalinina, V. Lyakhovetskii, C. Tondera, O. Gorsky, S. Moosavi, N. Pavlova, N. Merkulyeva, A. V. Kalueff, I. R. Minev, P. Musienko, *Nat. Biomed. Eng.* **2020**, *4*, 1010.
[20] F. Decataldo, T. Cramer, D. Martelli, I. Gualandi, W. Korim, S. Yao, M. Tessarolo, M. Murgia, E. Scavetta, R. Amici, B. Fraboni, *Sci. Rep.* **2019**, *9*, 10598.
[21] D. Khodagholy, T. Doublet, M. Gurfinkel, P. Quilichini, E. Ismailova, P. Leleux, T. Herve, S. Sanaur, C. Bernard, G. G. Malliaras, *Adv. Mater.* **2011**, *23*, H268.
[22] D. Khodagholy, J. N. Gelinas, T. Thesen, W. Doyle, O. Devinsky, G. G. Malliaras, G. Buzsáki, *Nat. Neurosci.* **2015**, *18*, 310.
[23] V. Paggi, O. Akouissi, S. Micera, S. P. Lacour, *J. Neural Eng.* **2021**, *18*, 031001.
[24] M. Silverå Ejneby, M. Jakešová, J. J. Ferrero, L. Migliaccio, I. Sahalianov, Z. Zhao, M. Berggren, D. Khodagholy, V. Đerek, J. N. Gelinas, E. D. Głowacki, *Nat. Biomed. Eng.* **2022**, *6*, 741.
[25] A. M. Cobo, C. E. Larson, K. Scholten, J. A. Miranda, S. Elyahoodayan, D. Song, V. Pikov, E. Meng, *J. Microelectromech. Syst.* **2019**, *28*, 36.
[26] C. M. Noller, Y. A. Levine, T. M. Urakov, J. P. Aronson, M. S. Nash, *Front. Neurosci.* **2019**, *13*, 911.
[27] M. Zhou, M. Huang, H. Zhong, C. Xing, Y. An, R. Zhu, Z. Jia, H. Qu, S. Zhu, S. Liu, L. Wang, H. Ma, Z. Qu, G. Ning, S. Feng, *Adv. Funct. Mater.* **2022**, *32*, 2200269.
[28] M. Sahin, M. A. Haxhiu, D. M. Durand, I. A. Dreshaj, *J. Appl. Physiol.* **1997**, *83*, 317.
[29] D. Terutsuki, H. Yoroizuka, S. Osawa, Y. Ogihara, H. Abe, A. Nakagawa, M. Iwasaki, M. Nishizawa, *Adv. Healthcare Mater.* **2022**, *11*, 2201627.
[30] R. Thakur, F. P. Aplin, G. Y. Fridman, *Micromachines* **2021**, *12*, 1522.
[31] C. C. Horn, M. Forssell, M. Sciullo, J. E. Harms, S. Fulton, C. Mou, F. Sun, T. W. Simpson, G. Xiao, L. E. Fisher, C. Bettinger, G. K. Fedder, *J. Neural Eng.* **2021**, *18*, 055008.
[32] D. R. Yao, H. Yu, O. J. Rauhala, C. Cea, Z. Zhao, J. N. Gelinas, D. Khodagholy, *Adv. Sci.* **2022**, *9*, e2104404.
[33] B. J. Woodington, V. F. Curto, Y.-L. Yu, H. Martínez-Domínguez, L. Coles, G. G. Malliaras, C. M. Proctor, D. G. Barone, *Sci. Adv.* **2021**, *7*, eabg7833.
[34] A. A. Sharp, H. V. Panchawagh, A. Ortega, R. Artale, S. Richardson-Burns, D. S. Finch, K. Gall, R. L. Mahajan, D. Restrepo, *J. Neural Eng.* **2006**, *3*, L23.

[35] Y. Zhang, N. Zheng, Y. Cao, F. Wang, P. Wang, Y. Ma, B. Lu, G. Hou, Z. Fang, Z. Liang, M. Yue, Y. Li, Y. Chen, J. Fu, J. Wu, T. Xie, X. Feng, *Sci. Adv.* **2019**, *5*, eaaw1066.
[36] M. Varga, M. Luniak, K. Wolter, in *2013 IEEE XXXIII Int. Scientific Conf. Electronics and Nanotechnology (ELNANO)*, IEEE, Piscatway, NJ, USA **2013**, p. 237–240.
[37] D. Karnaushenko, N. Münzenrieder, D. D. Karnaushenko, B. Koch, A. K. Meyer, S. Baunack, L. Petti, G. Tröster, D. Makarov, O. G. Schmidt, *Adv. Mater.* **2015**, *27*, 6797.
[38] M. Champeau, D. A. Heinze, T. N. Viana, E. R. d. Souza, A. C. Chinellato, S. Titotto, *Adv. Funct. Mater.* **2020**, *30*, 1910606.
[39] Y. Dong, S. Wang, Y. Ke, L. Ding, X. Zeng, S. Magdassi, Y. Long, *Adv. Mater. Technol.* **2020**, *5*, 2000034.
[40] T. F. Teshima, L. Hiendlmeier, K. Terkan, S. Zips, L. Grob, F. Zurita, P. Rinklin, B. Wolfrum, *Adv. Mater. Technol.* **2021**, *6*, 2100240.
[41] S. Tibbits, *Archit. Des.* **2014**, *84*, 116.
[42] A. Sydney Gladman, E. A. Matsumoto, R. G. Nuzzo, L. Mahadevan, J. A. Lewis, *Nat. Mater.* **2016**, *15*, 413.
[43] C. de, Kergariou, F. Demoly, A. Perriman, A. Le Duigou, F. Scarpa, *Adv. Funct. Mater.* **2022**, *33*, 2210353.
[44] L. Hiendlmeier, T. F. Teshima, F. Zurita, H. Url, P. Rinklin, B. Wolfrum, *Macromol. Mater. Eng.* **2022**, *307*, 2200306.
[45] G. Cortelli, L. Patruno, T. Cramer, M. Murgia, B. Fraboni, S. Miranda, *ACS Appl. Nano Mater.* **2021**, *4*, 8376.
[46] S. P. Lacour, D. Chan, S. Wagner, T. Li, Z. Suo, *Appl. Phys. Lett.* **2006**, *88*, 204103.
[47] A. Cisnal, J.-C. Fraile, J. Pérez-Turiel, V. Muñoz-Martinez, C. Müller, F. R. Ihmig, *Sensors* **2018**, *18*, 4152.
[48] S. F. Cogan, *Annu. Rev. Biomed. Eng.* **2008**, *10*, 275.
[49] M. Ganji, A. Tanaka, V. Gilja, E. Halgren, S. A. Dayeh, *Adv. Funct. Mater.* **2017**, *27*, 1703019.
[50] P. Oldroyd, J. Gurke, G. G Malliaras, *Adv. Funct. Mater.* **2022**, *33*, 2208881.
[51] M. Burrows, *J. Comp. Physiol.* **1995**, *176*, 289.
[52] S. Raspopovic, J. Carpaneto, E. Udina, X. Navarro, S. Micera, *J. NeuroEng. Rehab.* **2010**, *7*, 17.
[53] A. A. Szymanska, A. Hajirasooliha, Z. Nenadic, in 2013 6th Int. IEEE/EMBS Conf. on Neural Engineering (NER), IEEE, Piscataway, NJ, USA **2013**, pp. 235–238.
[54] G. Pollack, *J. Exp. Biol.* **1998**, *201*, 155.
[55] S. Zips, L. Hiendlmeier, L. J. K. Weiß, H. Url, T. F. Teshima, R. Schmid, M. Eblenkamp, P. Mela, B. Wolfrum, *ACS Appl. Polym. Mater.* **2021**, *3*, 243.
[56] J. T. Cabral, S. D. Hudson, C. Harrison, J. F. Douglas, *Langmuir* **2004**, *20*, 10020.
[57] Z. Zhao, J. Wu, X. Mu, H. Chen, H. J. Qi, D. Fang, *Sci. Adv.* **2017**, *3*, e1602326.
[58] F. Zurita, F. Del Duca, T. Teshima, L. Hiendlmeier, M. Gebhardt, H. Luksch, B. Wolfrum, *Sci. Rep.* **2022**, *12*, 10864.